J Appl Electrochem (2011) 41:99–106
DOI 10.1007/s10800-010-0213-8

ORIGINAL PAPER

Characteristics of lithium iron phosphate mixed with nano-sized acetylene black for rechargeable lithium-ion batteries

Guoen Sun · Bo Jin · Guangping Sun · Enmei Jin · Hal-Bon Gu · Qing Jiang

Received: 1 January 2010 / Accepted: 5 September 2010 / Published online: 22 September 2010

Abstract Lithium iron phosphate mixed with nano-sized acetylene black ($LiFePO_4$-AB) was synthesized by a hydrothermal method and subsequent high-energy ball-milling process. Different contents of AB were added to improve the electronic conductivity of $LiFePO_4$. The structural and morphological performance of $LiFePO_4$-AB was investigated by X-ray diffraction (XRD), Raman spectroscopy, scanning electron microscope, and high-resolution transmission electron microscope. $LiFePO_4$-AB/Li batteries were fabricated in an argon-filled glove box, and their electrochemical performance was analyzed by cyclic voltammetry and charge/discharge tests. The XRD results demonstrate that $LiFePO_4$-AB has an olivine-type structure indexed to the orthorhombic *Pnma* space group. $LiFePO_4$-AB/Li battery with 10 wt% AB shows the best high-rate discharge properties with the discharge capacities of 116 mAh g^{-1} at 1 C and 85 mAh g^{-1} at 10 C at room temperature.

Keywords Lithium iron phosphate · Lithium-ion batteries · High-rate

1 Introduction

Rechargeable lithium-ion batteries as one of the most important power sources are in a variety of applications such as mobile phones, laptop computers, and digital cameras because they offer relatively high specific capacity compared with conventional batteries [1]. In the rechargeable lithium-ion batteries, a cathode material is a key component, and mainly devoted to the performance of the batteries. Among the well-known cathode materials, layered $LiCoO_2$ and $LiNiO_2$, spinel $LiMn_2O_4$, and other cathode materials such as elemental sulfur have been studied extensively [2–8]. Nowadays, $LiCoO_2$ has been used as a cathode material for commercial lithium-ion batteries. However, due to the toxicity and the high cost of cobalt, novel cathode material must be developed not only in relation to battery performance but also in relation to safety and cost especially in the applications of electrical vehicles and hybrid electrical vehicles.

Recently, lithium transition metal phosphates proposed by Goodenough et al. [9–19] with ordered olivine-type structures, $LiMPO_4$ (where M = Fe, Mn, Ni, or Co), have attracted extensive attention as lithium insertion cathode materials for the next generation of rechargeable lithium-ion batteries. Among these phosphates, $LiFePO_4$ is the most attractive because of its high stability, low cost, and high compatibility with environment. However, it is difficult to attain its full capacity because its electronic conductivity is very low, which leads to initial capacity loss and poor rate capability, and diffusion of Li^+ ion across the $LiFePO_4/FePO_4$ boundary is slow due to its intrinsic character [9]. The electronic conductivity of $LiFePO_4$ is only 10^{-9} S cm^{-1}, as demonstrated previously by us [20], which is much lower than those of $LiCoO_2$ ($\sim 10^{-3}$ S cm^{-1}) [21] and $LiMn_2O_4$ (2×10^{-5} to 5×10^{-5} S cm^{-1}) [22]. There are two methods to improve the electronic conductivity. One is to introduce conductive additives including carbon coating [23] and supervalent cation doping [24]. The other is to control particle size by optimizing synthesis conditions

G. Sun · B. Jin (✉) · G. Sun · Q. Jiang
Key Laboratory of Automobile Materials, Ministry of Education, and School of Materials Science and Engineering, Jilin University, Changchun 130025, China
e-mail: jinbo@jlu.edu.cn

E. Jin · H.-B. Gu
Department of Electrical Engineering, Chonnam National University, Gwangju 500-757, South Korea

[25, 26]. In the previous literatures, $LiFePO_4$ was mainly synthesized by solid-state reaction [27, 28] and sol–gel method [29, 30]. The solid-state reaction as a commercial large-scale synthesis method usually needs high firing temperature and long firing time, and can not produce nano-sized powders. The sol–gel method can prepare sub-micron powders, but the preparation process is usually difficult to control. Herein, we use a hydrothermal method to synthesize $LiFePO_4$. It is a useful method to prepare fine particles, and has some advantages such as simple synthesis process and low energy consumption.

It is universally known that high-energy ball-milling process is a promising method for synthesizing cathode materials [31]. During the high-energy ball-milling process, the powder particles undergo repeated welding, fracturing, and re-welding in a dry high-energy ball-milling vessel, which results in pulverization and intimate powder mixing. An improvement in electronic conductivity of $LiFePO_4$-AB prepared by the high-energy ball-milling process can be expected due to the very fine nanoparticles and their large specific surface area.

In this study, therefore, we use the hydrothermal method and subsequent high-energy ball-milling process to prepare $LiFePO_4$ mixed with nano-sized acetylene black ($LiFePO_4$-AB). The purpose of adding AB is to improve the electronic conductivity of $LiFePO_4$. The structural and morphological performance of $LiFePO_4$-AB was analyzed by means of scanning electron microscope (SEM), high-resolution transmission electron microscope (HR-TEM), X-ray diffraction (XRD) and Raman spectroscopy. The electrochemical performance of $LiFePO_4$-AB/Li batteries was analyzed by cyclic voltammetry and charge/discharge tests.

2 Experimental

$LiFePO_4$ synthesized hydrothermally at 170 °C for 10 h without ball-milling and without annealing further at 500 °C for 1 h was prepared from $LiOH{\cdot}H_2O$ (Aldrich 99.95%), $FeSO_4{\cdot}7H_2O$ (Aldrich 99%), $(NH_4)_3PO_4{\cdot}3H_2O$ (Wako 99%), and $C_6H_8O_6$ (Aldrich 99%), as described previously by us [32]. To improve low electronic conductivity of $LiFePO_4$, nano-sized AB (Chevron Chemical Co., average particle size: 50 nm, 5, 10, or 15 wt%) was added into the solution of the obtained $LiFePO_4$ and *N*-methylpyrrolidinone (NMP), and then the mixture was ball-milled for 10 h using a shaker type of ball mill (Planetary Mono Mill). The ball-to-powder weight ratio was 20:1. After drying at 90 °C for 12 h, the powders were pelleted and further heated at 500 °C for 1 h in nitrogen atmosphere. After cooling to room temperature, the mixture of NMP and $LiFePO_4$-AB was ball-milled again for 10 h. Finally, the mixture was dried at 90 °C for 12 h. For comparison, pure $LiFePO_4$ were also prepared by the hydrothermal method followed by subsequent high-energy ball-milling and heat-treating at the same procedure.

The crystalline phases were identified with XRD (Dmax/1200, Rigaku) with Cu Kα radiation ($\lambda = 1.5406$ Å) and the powder morphologies were observed by SEM (JEOL JSM-5400) and high-resolution transmission electron microscope (HR-TEM, Philips, Tecnai F20). Raman spectroscopy was carried out on a Jobin–Yvon LabRam HR800. The 514 nm argon-ion laser as excitation radiation was focused onto the surface of the powders by the 100× objective lens, and the laser power was set to ca. 10 mW to avoid heating or radiation damage to the samples.

The composite electrodes were prepared by mixing as-prepared pure $LiFePO_4$ or $LiFePO_4$-AB with carbon black and polyvinylidene fluoride in a weight ratio of 70:25:5 in NMP. The slurry was coated onto aluminum foil and dried at 90 °C for 1 h before roll-pressing, and then the electrodes were cut into 2 × 2 cm sections and dried again at 110 °C for 24 h under vacuum. The beaker-type batteries were assembled in an argon-filled glove box using lithium as the anode and 1 M $LiPF_6$ dissolved in ethylene carbonate/dimethyl carbonate (1:1) as the electrolyte. The charge/discharge tests were performed using automatic charge/discharge equipment (WBCS3000, WonATech) in a potential range of 2.0–4.5 V at various C-rates ranging from C/10 to 10 C (1 C = 170 mA g^{-1}) at room temperature. The WBCS3000 battery tester system was also used for measurements of CV at a scan rate of 0.1 mV s^{-1} from 2.0 to 4.5 V. The electronic conductivity of the samples was measured by four-point probe method.

3 Results and discussion

The XRD patterns for pure $LiFePO_4$ and $LiFePO_4$-AB with different AB contents are shown in Fig. 1. The diffraction patterns demonstrate that both pure $LiFePO_4$ and $LiFePO_4$-AB are a kind of single-phase material having an olivine-type structure indexed to the orthorhombic *Pnma* space group, it is the same as the one that is listed in the X-ray powder diffraction data file (JCPDS card number 81-1173) as standard. The crystallite sizes (D) of pure $LiFePO_4$ and $LiFePO_4$-AB were calculated by the Scherrer's equation: $D = 0.9\lambda/\beta\cos\theta$ from the full-width-at-half-maximum β of four strong and well-resolved reflection peaks corresponding to (101), (111), (211), and (311) crystallographic directions and the mean value was calculated [33, 34]. As shown in Table 1, $D = 34$ nm for pure $LiFePO_4$, $D = 22$ nm for $LiFePO_4$-AB_5, $D = 17$ nm for $LiFePO_4$-AB_{10}, and $D = 20$ nm for $LiFePO_4$-AB_{15}, respectively where the subscripts of AB denote wt% AB, and $LiFePO_4$-AB_{10} has the smallest crystallite size. In pure $LiFePO_4$ and $LiFePO_4$-AB, there are

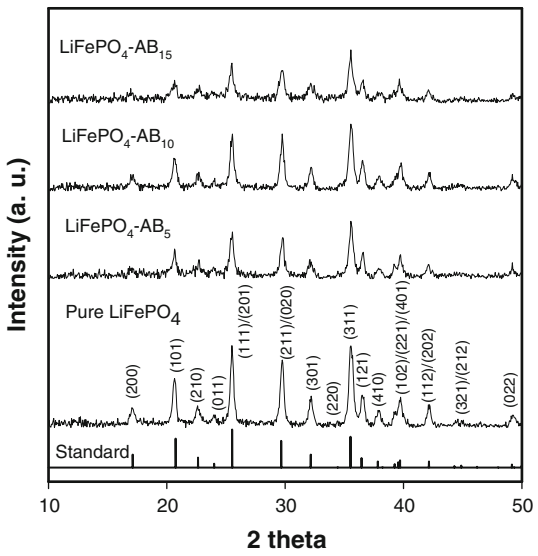

Fig. 1 XRD patterns for pure $LiFePO_4$, $LiFePO_4$-AB_5, $LiFePO_4$-AB_{10}, and $LiFePO_4$-AB_{15}

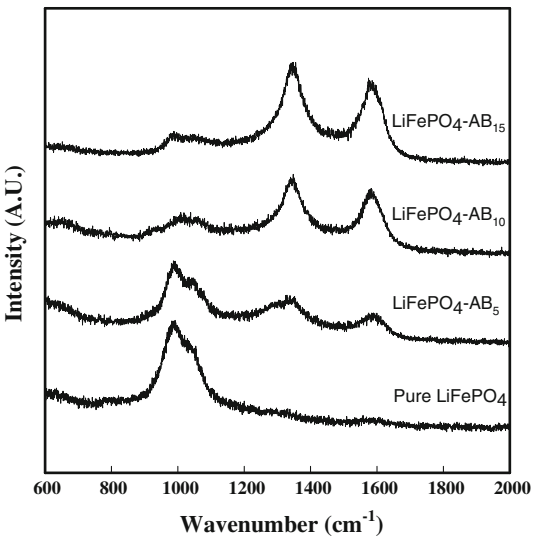

Fig. 2 Raman spectra of pure $LiFePO_4$, $LiFePO_4$-AB_5, $LiFePO_4$-AB_{10}, and $LiFePO_4$-AB_{15}

Table 1 The lattice constants of $LiFePO_4$-AB with different AB contents calculated from the XRD patterns

Cell constants	$LiFePO_4$	$LiFePO_4$-AB_5	$LiFePO_4$-AB_{10}	$LiFePO_4$-AB_{15}
a (Å)	10.3037	10.5230	10.3404	10.4614
b (Å)	5.9808	5.9960	6.0058	5.9960
c (Å)	4.6977	4.7127	4.7434	4.7183
V (Å^3)	289.49	297.35	294.58	295.96

no Fe^{3+} impurities. The addition of L-ascorbic acid ($C_6H_8O_6$) as a reducing agent to the precursor is useful in prohibiting the conversion of Fe^{2+} to Fe^{3+} during the hydrothermal reaction. As demonstrated in Table 1, the lattice parameters '*a*', '*b*', and '*c*' of $LiFePO_4$-AB_5, $LiFePO_4$-AB_{10}, and $LiFePO_4$-AB_{15} slightly increase compared to pure $LiFePO_4$, but they do not lead to the change in the crystal structure of $LiFePO_4$-AB.

Raman spectra of pure $LiFePO_4$ and $LiFePO_4$-AB with different AB contents are shown in Fig. 2. As can be seen from Fig. 2, in $LiFePO_4$-AB_5, $LiFePO_4$-AB_{10}, and $LiFePO_4$-AB_{15}, typical D (sp^3-type) and G (sp^2-type) bands of carbon are located in ca. 1338 and 1585 cm^{-1}, respectively; these bands are due to carbon originated from the added AB on the surface of $LiFePO_4$ particles. The D and G band intensities of these samples increase upon AB content increasing. Graphite can generally crystallize according to D_{6h} space group that is associated with vibrational modes of irreducible representation ($A_{2u} + 2B_{2g} + E_{1u} + 2E_{2g}$) [35], and the E_{2g} modes at 42 and 1581 cm^{-1} are Raman-active [36]. G band (1585 cm^{-1}) is assigned to the E_{2g} graphite mode, and D band (1338 cm^{-1}) is associated to A_{1g} mode, which is related to the breakage of symmetry occurring at the edges of graphite sheets [37]. The bands at ca. 1585 and 1338 cm^{-1} are originated from graphitic and amorphous forms, respectively. In all cases, a band at ca. 950 cm^{-1} is assigned to the A_g mode of the totally symmetric stretching vibrations of the PO_4^{3-} in $LiFePO_4$, and its intensity decreases upon AB content increasing. For pure $LiFePO_4$, there are no D and G bands of carbon due to its low content.

The SEM images of pure $LiFePO_4$ and $LiFePO_4$-AB with different AB contents are shown in Fig. 3. As shown in Fig. 3, the particle size of pure $LiFePO_4$ is around 50–200 nm, around 50–100 nm for $LiFePO_4$-AB_5, around 20–100 nm for $LiFePO_4$-AB_{10} and around 50–150 nm for $LiFePO_4$-AB_{15}, respectively, where $LiFePO_4$-AB_{10} has the smallest particle size. $LiFePO_4$ nanoparticles are connected each other by carbon, and the dispersed AB provides pathways for electron transference. Therefore, the electronic conductivity of $LiFePO_4$-AB is improved. As shown in Table 2, the electronic conductivity $\sigma = 5.86 \times 10^{-9}$ S cm^{-1} for $LiFePO_4$, $\sigma = 8.00 \times 10^{-5}$ S cm^{-1} for $LiFePO_4$-AB_5, $\sigma = 7.85 \times 10^{-4}$ S cm^{-1} for $LiFePO_4$-AB_{10}, and $\sigma = 2.71 \times 10^{-2}$ S cm^{-1} for $LiFePO_4$-AB_{15}, respectively. It is obvious that σ increases as the AB content increases.

The SEM image obtained for $LiFePO_4$-AB_{10} and the corresponding elemental mapping of P, Fe, and C are presented in Fig. 4. The images of elements P, Fe, and C closely match with the corresponding SEM image, indicating the homogenous chemical composition of the sample. Since carbon also follows the same uniform distribution as that of the two elements, it is concluded that

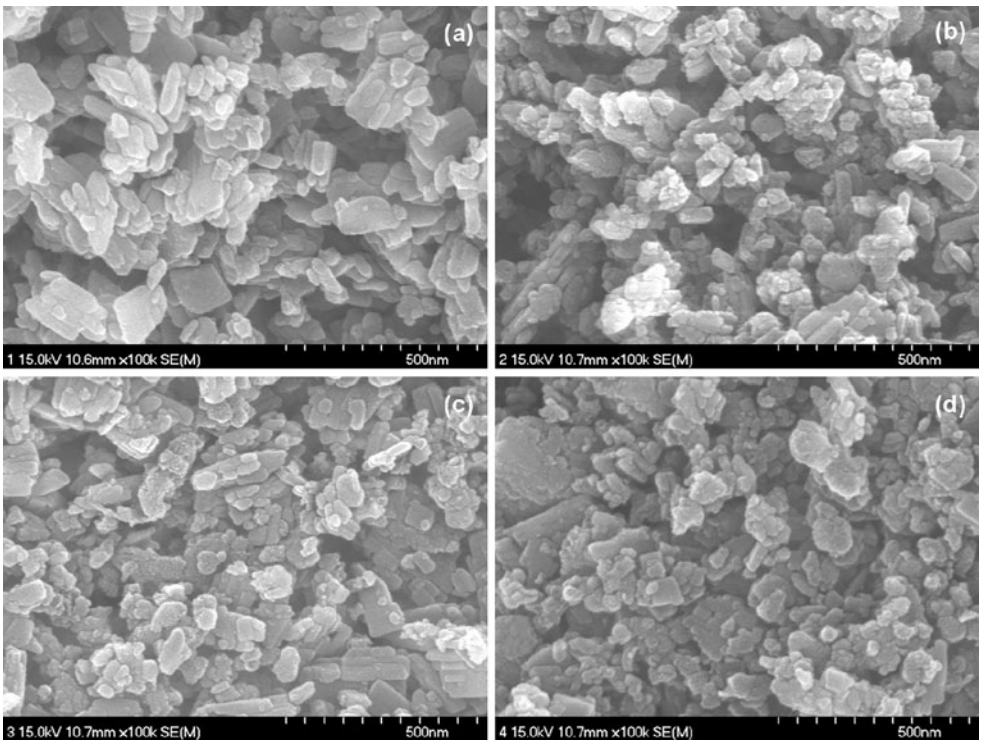

Fig. 3 SEM images of **a** pure $LiFePO_4$, **b** $LiFePO_4$-AB_5, **c** $LiFePO_4$-AB_{10}, and **d** $LiFePO_4$-AB_{15}

Table 2 The properties of $LiFePO_4$-AB with different AB contents

	$LiFePO_4$	$LiFePO_4$-AB_5	$LiFePO_4$-AB_{10}	$LiFePO_4$-AB_{15}
Average crystallite size[a] (nm)	34	22	17	20
Particle size range[b] (nm)	50–200	50–100	20–100	50–150
Electronic conductivity (S cm^{-1})	5.86×10^{-9}	8.00×10^{-5}	7.85×10^{-4}	2.71×10^{-2}

[a] Calculated from XRD data

[b] Estimated from SEM data

$LiFePO_4$-AB contains carbon in a uniformly dispersed manner.

The HR-TEM images of $LiFePO_4$-AB with different AB contents are shown in Fig. 5. It is found that about 1–5 nm thick and amorphous layer is coated on the particle surface for all the $LiFePO_4$-AB powders. This is due to the added AB and the generated carbon on the particle surface through decomposition of $C_6H_8O_6$ during the heat treatment. In our previous study [32], we have demonstrated that there is about 1–3 nm thick and amorphous layer coated on pure $LiFePO_4$ surface due to the generated carbon on the particle surface through decomposition of $C_6H_8O_6$ during the heat treatment.

The cyclic voltammetry of $LiFePO_4$/Li and $LiFePO_4$-AB/Li batteries with different AB contents in the first cycle at a scan rate of 0.1 mV s^{-1} is shown in Fig. 6. As shown in Fig. 6, the oxidation and reduction peaks of $LiFePO_4$/Li battery appear at about 3.56 and 3.28 V, respectively, and the potential interval between two peaks is 0.28 V. All the three pairs of oxidation and reduction peaks of $LiFePO_4$-AB_5/Li, $LiFePO_4$-AB_{10}/Li, and $LiFePO_4$-AB_{15}/Li batteries appear at about 3.5 and 3.35 V, respectively, and the potential interval between the oxidation and reduction peak is 0.15 V, being obviously smaller than that of $LiFePO_4$/Li battery. The intensities of oxidation and reduction peaks for $LiFePO_4$-AB_{10}/Li battery are the largest compared to the other samples. In the meantime, the redox peak profiles of $LiFePO_4$-AB_5/Li, $LiFePO_4$-AB_{10}/Li, and $LiFePO_4$-AB_{15}/Li batteries are more symmetric and spiculate than that of $LiFePO_4$/Li battery, indicating that the reversibility and reactivity of $LiFePO_4$-AB/Li batteries are better than that of $LiFePO_4$/Li battery.

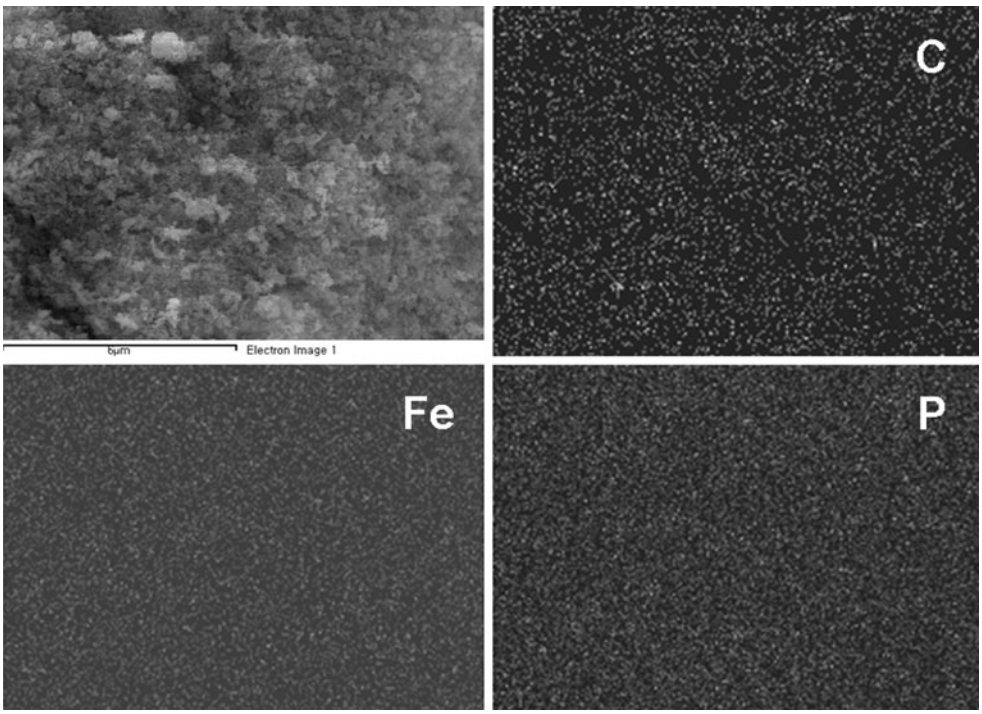

Fig. 4 SEM image of $LiFePO_4$-AB_{10} and the corresponding elemental mapping of P, Fe, and C

It is well known that the electrochemical process of $LiFePO_4$ described as two-phase redox reaction is as follows,

$$LiFePO_4 - xLi^+ - xe^- \Leftrightarrow (1-x)LiFePO_4 + xFePO_4$$

where the maximum exchange of 1 mol of Li per formula unit ($x = 1$) corresponds to a theoretical specific capacity of 170 mAh g^{-1}.

The initial discharge curves of $LiFePO_4$/Li and $LiFePO_4$-AB_{10}/Li batteries at different discharge C-rates are shown in Fig. 7. The batteries are first charged/discharged several times at C/5, and then the charge/discharge tests at various C-rates ranging from 1 C to 10 C in a potential range of 2.0–4.5 V at room temperature were performed. The characteristic flat discharge plateau at around 3.4 V, which represents a two-phase reaction in the electrode, is observed for two samples. As for $LiFePO_4$/Li battery, the initial discharge capacities obtained at 1, 3, 5, and 10 C are 111, 75, 53, and 26 mAh g^{-1}, respectively, and the amount of cycled lithium $x = 0.65$, 0.44, 0.31, and 0.15, respectively. The potential plateau remains flat even for the 3 C curve except for a slight decrease. However, in the case of $LiFePO_4$-AB_{10}/Li battery, the initial discharge capacities obtained at 1, 3, 5, and 10 C are 116, 103, 96, and 85 mAh g^{-1}, respectively, and the amount of cycled lithium $x = 0.68$, 0.61, 0.56, and 0.5, respectively. The potential plateau remains flat even for the 10 C curve except for a slight decrease. In light of the above results, it is concluded that the battery may operate at relatively high rates up to 10 C, confirming the improved kinetics of $LiFePO_4$-AB_{10}. In all cases, the initial discharge capacity decreases while the over-potential increases with the C-rate increasing. This phenomenon can be explained in terms of the electric polarization due to an increase in the *IR* drop, where *I* is the current passing the battery and *R* is the battery impedance.

According to the results in Fig. 7, we can demonstrate the relation between the initial discharge capacity and the discharge rate for $LiFePO_4$/Li and $LiFePO_4$-AB_{10}/Li batteries, as shown in Fig. 8. It is obvious that the discharge rate capability of $LiFePO_4$-AB_{10}/Li battery is better than that of $LiFePO_4$/Li due to an increase in the electronic conductivity and a decrease in crystallite size *D* of $LiFePO_4$-AB_{10}, as demonstrated in Table 2. The crystallite size *D* has an important effect on the transport of lithium ions and electrons into and out of the individual crystal. The smaller the crystallite size *D*, the greater the efficiency of the full conversion of $LiFePO_4$ to $FePO_4$, inducing an increase in the capacity.

The cycling performance of $LiFePO_4$/Li and $LiFePO_4$-AB/Li batteries with different AB contents at a discharge rate of 3 C/10 is shown in Fig. 9. The batteries are firstly charged/discharged several times at C/5, and then the charge/discharge tests at various C-rates ranging from 1 to 10 C in a potential range of 2.0–4.5 V at room temperature were performed, and the results are presented in Fig. 10.

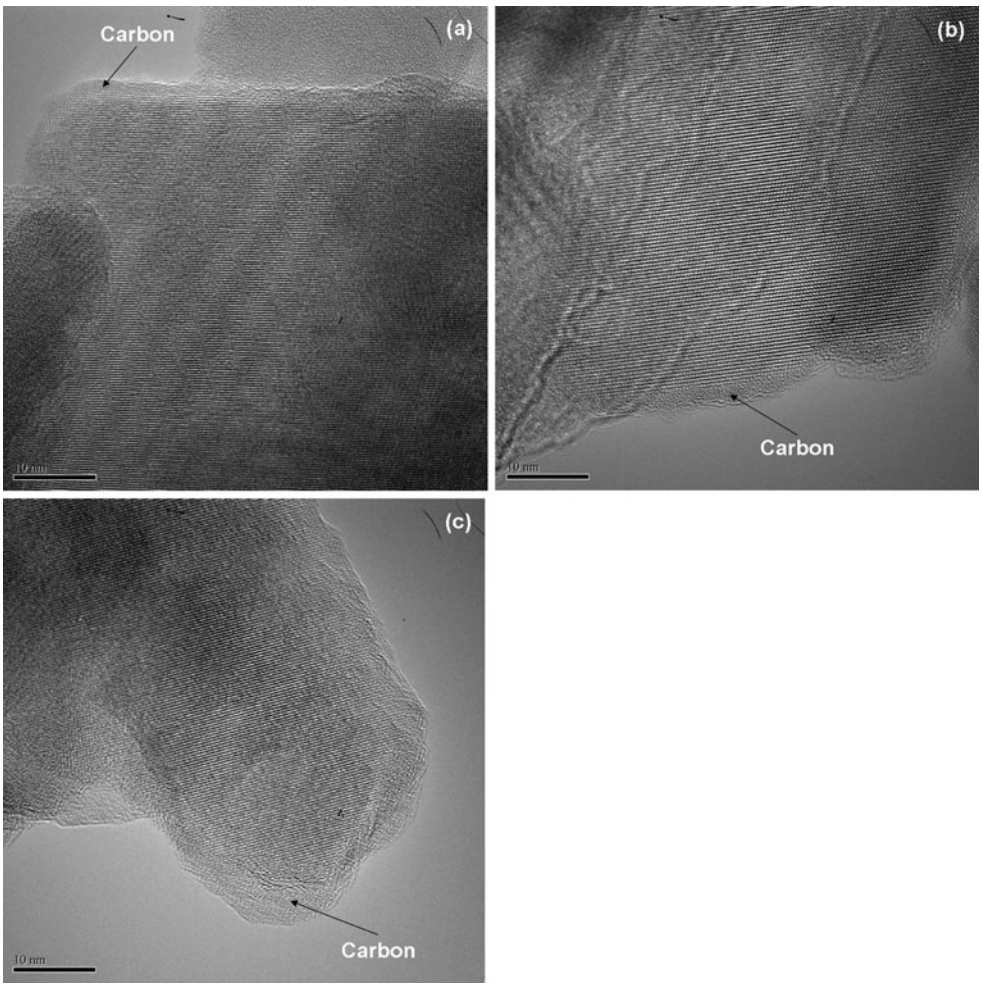

Fig. 5 HR-TEM images of **a** $LiFePO_4$-AB_5, **b** $LiFePO_4$-AB_{10}, and **c** $LiFePO_4$-AB_{15}

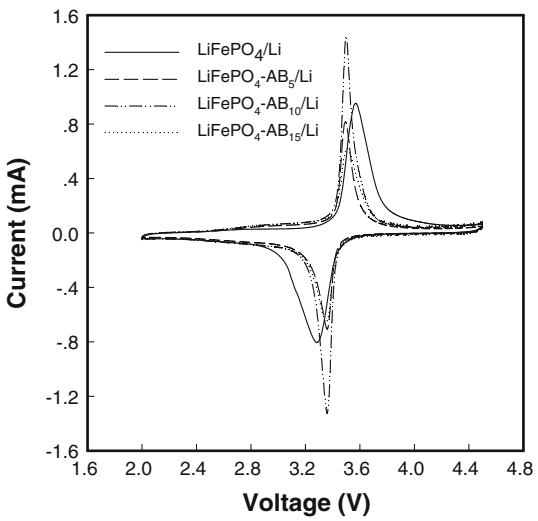

Fig. 6 The cyclic voltammograms of $LiFePO_4$/Li, $LiFePO_4$-AB_5/Li, $LiFePO_4$-AB_{10}/Li, and $LiFePO_4$-AB_{15}/Li batteries in the first cycle at a scan rate of 0.1 mV S^{-1}

As shown in Fig. 9, the discharge capacity of $LiFePO_4$/Li battery is 129 mAh g^{-1} in the first cycle, subsequently decreases to 120 mAh g^{-1} after 30 cycles, indicating a decrease in the discharge capacity upon cycling due to the slow diffusion of lithium ions in the $LiFePO_4$. The initial discharge capacities of $LiFePO_4$-AB_5/Li, $LiFePO_4$-AB_{10}/Li, and $LiFePO_4$-AB_{15}/Li batteries are 131, 144, and 129 mAh g^{-1}, respectively; after 30 cycles, the discharge capacities remain no change. It is demonstrated that $LiFePO_4$-AB/Li batteries display excellent capacity retention and cycling performance of $LiFePO_4$-AB_{10}/Li battery is the best, which is consistent with the results of XRD in Fig. 1, SEM in Fig. 3, and the CV in Fig. 6, in the meantime, and also depends on an increase in electronic conductivity of $LiFePO_4$-AB, as demonstrated in Table 2. As shown in Fig. 10, although the discharge capacities of both $LiFePO_4$/Li and $LiFePO_4$-AB_{10}/Li batteries decrease with the C-rate increasing, and can completely recover to the initial value when the discharge rate changes back to 1 C,

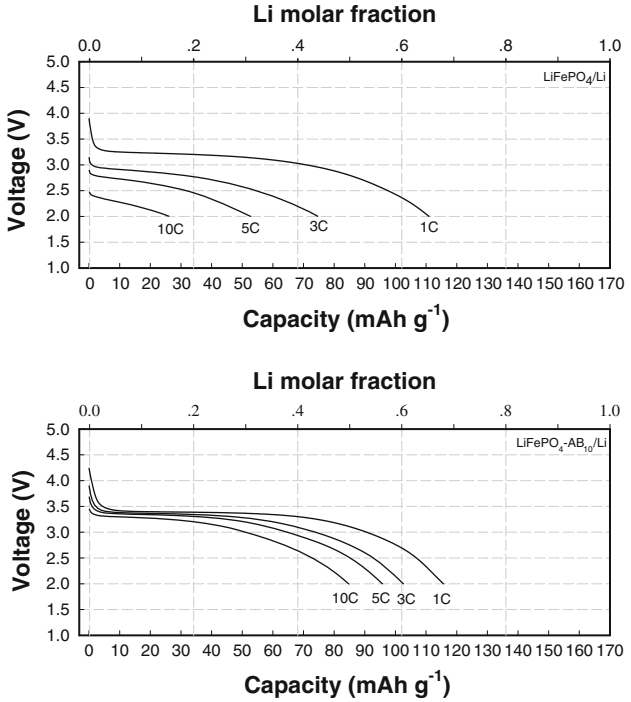

Fig. 7 The initial discharge curves of $LiFePO_4$/Li and $LiFePO_4$-AB_{10}/Li batteries at various C-rates ranging from 1 to 10 C at room temperature

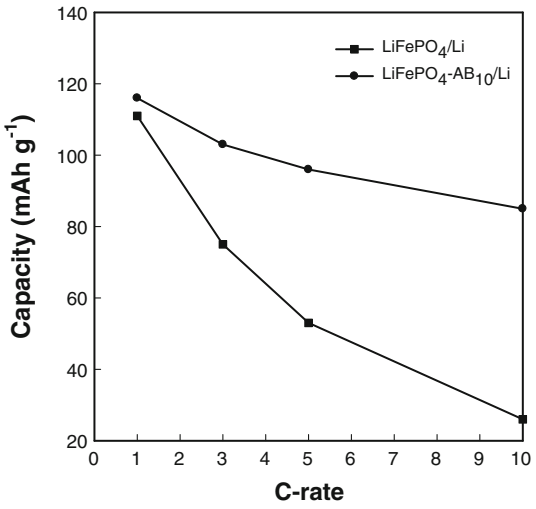

Fig. 8 The relation between the initial discharge capacity and the discharge rate for $LiFePO_4$/Li and $LiFePO_4$-AB_{10}/Li batteries

indicating that both $LiFePO_4$ and $LiFePO_4$-AB_{10} have excellent electrochemical reversibility and structural stability. Figure 10 also demonstrates that $LiFePO_4$-AB_{10}/Li battery exhibits better capacity retention than $LiFePO_4$/Li battery especially at high-rate.

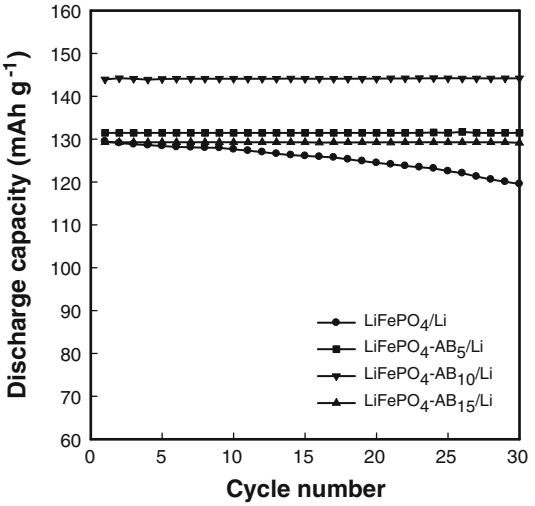

Fig. 9 The cycling performance of $LiFePO_4$/Li, $LiFePO_4$-AB_5/Li, $LiFePO_4$-AB_{10}/Li, and $LiFePO_4$-AB_{15}/Li batteries at 3 C/10 at room temperature

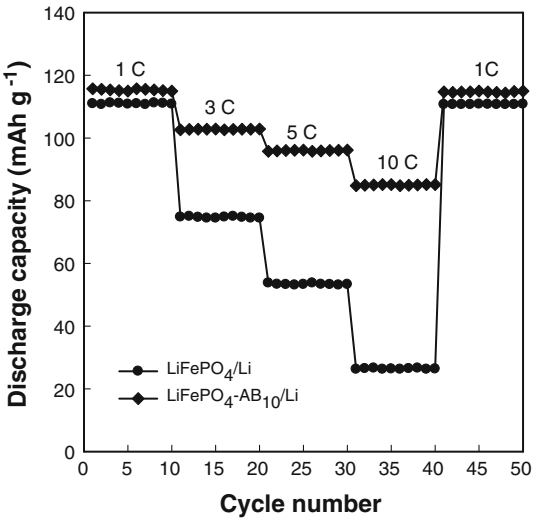

Fig. 10 The cycling performance of $LiFePO_4$/Li and $LiFePO_4$-AB_{10}/Li batteries at various C-rates ranging from 1 to 10 C at room temperature

4 Conclusions

$LiFePO_4$-AB has been synthesized successfully by the hydrothermal method and subsequent high-energy ball-milling process. The XRD results demonstrate that $LiFePO_4$-AB has an olivine-type structure indexed to the orthorhombic *Pnma* space group. $LiFePO_4$-AB_{10}/Li battery shows the best high-rate discharge properties with the discharge capacities of 116 mAh g^{-1} at 1 C and 85 mAh g^{-1} at 10 C at room temperature.

Acknowledgments The authors acknowledge the financial supports from National Key Basic Research and Development Program of China (Grant No. 2010CB631001) and the China Postdoctoral

Science Foundation Funded Project (Grant No. 20090451124). This research project also receives supporting funds from the second-stage Brain Korea 21.

References

1. Tarascon J-M, Armand M (2001) Nature 414:359
2. Gu YX, Chen DR, Jiao XL (2005) J Phys Chem B 109:17901
3. Sauvage F, Tarascon J-M, Baudrin E (2007) J Phys Chem C 111:9264
4. Zheng HH, Zhang HC, Fu YB, Abe T, Ogumi Z (2005) J Phys Chem B 109:13676
5. Luo JY, Wang YG, Xiong HM, Xia YY (2007) Chem Mater 19:4791
6. Lee HC, Chang S-K, Goh E-Y, Jeong J-Y, Lee JH, Kim H-J, Cho J-J, Hong S-T (2008) Chem Mater 20:5
7. Jin B, Kim J-U, Gu H-B (2003) J Power Sources 117:148
8. Jayalakshmi M, Rao MM, Scholz F (2003) Langmuir 19:8403
9. Padhi AK, Nanjundaswamy KS, Goodenough JB (1997) J Electrochem Soc 144:1188
10. Hu YS, Guo YG, Dominko R, Gaberscek M, Jamnik J, Maier J (2007) Adv Mater 19:1963
11. Aldon L, Perea A, Womes M, Ionica-Bousquet CM, Jumas J-C (2010) J Solid State Chem 183:218
12. Wang Y, Wang J, Yang J, Nuli Y (2006) Adv Funct Mater 16:2135
13. Fisher CAJ, Prieto VMH, Islam MS (2008) Chem Mater 20:5907
14. Delacourt C, Poizot P, Morcrette M, Tarascon J-M, Masquelier C (2004) Chem Mater 16:93
15. Wang LN, Li ZC, Xu HJ, Zhang KL (2008) J Phys Chem C 112:308
16. Bramnik NN, Nikolowski K, Baehtz C, Bramnik KG, Ehrenberg H (2007) Chem Mater 19:908
17. Zaghib K, Mauger A, Goodenough JB, Gendron F, Julien CM (2007) Chem Mater 19:3740
18. Amine K, Yasuda H, Yamachi M (2000) Electrochem Solid State Lett 3:178
19. Islam MS, Driscoll DJ, Fisher CAJ, Slater PR (2005) Chem Mater 17:5085
20. Jin B, Jin EM, Park K-H, Gu H-B (2008) Electrochem Commun 10:1537
21. Molenda J, Stoklosa A, Bak T (1989) Solid State Ion 36:53
22. Shimakawas Y, Numata T, Tabuchi J (1997) J Solid State Chem 131:138
23. Gabrisch H, Wilcox JD, Doeff MM (2006) Electrochem Solid-State Lett 9:A360
24. Chung S-Y, Bloking JT, Chiang Y-M (2002) Nat Mater 1:123
25. Yamada A, Chung SC, Hinikuma K (2001) J Electrochem Soc 148:A224
26. Gibot P, Cabanas MC, Laffont L, Levasseur S, Carlach P, Hamelet S, Tarascon J-M, Masquelier C (2008) Nat Mater 7:741
27. Meethong N, Huang H-YS, Speakman SA, Carter WC, Chiang Y-M (2007) Adv Funct Mater 17:1115
28. Stevens R, Dodd JL, Kresch MG, Yazami R, Fultz B, Ellis B, Nazar LF (2006) J Phys Chem B 110:22732
29. Dominko R, Bele M, Goupil J-M, Gaberscek M, Hanzel D, Arcon I, Jamnik J (2007) Chem Mater 19:2960
30. Giorgetti M, Berrettoni M, Scaccia S, Passerini S (2006) Inorg Chem 45:2750
31. Franger S, Cras FL, Bourbon C, Rounault H (2002) Electrochem Solid-State Lett 5:A231
32. Jin B, Gu H-B (2008) Solid State Ion 178:1907
33. Sanchez MAE, Brito GES, Fantini MCA, Goya GF, Matos JR (2006) Solid State Ion 177:497
34. Arnold G, Garche J, Hemmer R, Strobele S, Volger C, Wohlfahrt-Mehrens M (2003) J Power Sources 119–121:247
35. Tuinstra F, Koenig JL (1970) J Chem Phys 53:1126
36. Sinha K, Menédez J (1990) Phys Rev B 41:10845
37. Palomares V, Goñi A, de Muro IGil, de Meatza I, Bengoechea M, Cantero I, Rojo T (2010) J Power Sources 195:7661